ARCHIVIO ISTITUZIONALE
DELLA RICERCA

Alma Mater Studiorum Università di Bologna
Archivio istituzionale della ricerca

A multiple scattering formulation for finite-size flexural metasurfaces

This is the final peer-reviewed author's accepted manuscript (postprint) of the following publication:

Published Version:
Xingbo Pu, Antonio Palermo, Alessandro Marzani (2022). A multiple scattering formulation for finite-size flexural metasurfaces. PROCEEDINGS OF THE ROYAL SOCIETY OF LONDON. SERIES A, 478(2262), 1-19 [10.1098/rspa.2021.0669].

Availability:
This version is available at: https://hdl.handle.net/11585/897228 since: 2022-10-25

Published:

DOI: http://doi.org/10.1098/rspa.2021.0669

Terms of use:

Some rights reserved. The terms and conditions for the reuse of this version of the manuscript are specified in the publishing policy. For all terms of use and more information see the publisher's website.

This item was downloaded from IRIS Università di Bologna (https://cris.unibo.it/).
When citing, please refer to the published version.

(Article begins on next page)

27 January 2025

PROCEEDINGS A

rspa.royalsocietypublishing.org

Research

Article submitted to journal

Subject Areas:
Mechanics, wave motion

Keywords:
Elastic metamaterials, Rayleigh waves, Lamb's problem, Seismic metasurfaces, Structure-soil-structure interactions

Author for correspondence:
Alessandro Marzani
e-mail: alessandro.marzani@unibo.it
Antonio Palermo
e-mail: antonio.palermo6@unibo.it

A multiple scattering formulation for finite-size flexural metasurfaces

Xingbo Pu, Antonio Palermo and Alessandro Marzani

Department of Civil, Chemical, Environmental and Materials Engineering, University of Bologna, 40136 Bologna, Italy

We provide an analytical formulation to model the propagation of elastic waves in a homogeneous half-space supporting an array of thin plates. The technique provides the displacement field obtained from the interaction between an incident wave generated by a harmonic source and the scattered fields induced by the flexural motion of the plates. The scattered field generated by each plate is calculated using an ad-hoc set of Green's functions. The interaction between the incident field and the scattered fields is modelled through a multiple scattering formulation. Owing to the introduction of the multiple scattering formalism, the proposed technique can handle a generic set of plates arbitrarily arranged on the half-space surface. The method is validated via comparison with finite element simulations considering Rayleigh waves interacting with a single and a collection of thin plates. Our framework can be used to investigate the interaction of vertically polarized surface waves and flexural resonators in different engineering contexts, from the design of novel surface acoustic wave devices to the interpretation of urban vibrations problems.

1. Introduction

In the past two decades, the advent of so-called metamaterials, structured materials equipped with resonant elements, has opened new horizons in the control of waves across different physics. In elastodynamics, architected materials with unique effective properties such as negative density and negative moduli have shown the capability of tailoring the wavefields at will [1].

© The Authors. Published by the Royal Society under the terms of the Creative Commons Attribution License http://creativecommons.org/licenses/by/4.0/, which permits unrestricted use, provided the original author and source are credited.

THE ROYAL SOCIETY PUBLISHING

At their conception, elastic metamaterials were designed to filter the propagation of bulk waves [2]. However, the fabrication of resonant elements in the host medium challenges the feasibility of large-scale samples and eventually disrupts the integrity of the hosting material to some extent [3].

These issues were partially mitigated by the design of elastic metasurfaces, thin resonant interfaces comprising subwavelength resonant elements located on the surface of the waveguides [4–7]. Nowadays, metasurfaces are proposed to manipulate waves across a wide range of scales, from micro-mechanical systems [8] to ground-vibration mitigation devices [6,9,10]. In all these contexts, the dispersion relation, a function of angular frequency ω and wavenumber k, plays an important role in describing the dynamics of infinite metasurfaces. Knowledge of the dispersion curves provides physical insights on the existence of bandgaps, modes hybridization phenomena, cut-on and cut-off frequencies of an infinite length system. Dispersion relations of metasurfaces can be computed either via analytical formulations, by modelling the thin resonant interface as dynamic boundary conditions (BCs) [4,11], or via finite element (FE) schemes by modelling a finite size portion of the system including the substrate and the metasurface and by imposing proper periodic BCs [12–14]. The analytical formulations often exploit homogenization and asymptotic expansion techniques to obtain closed-form dispersion relation for compressional (rod-like) [6,15] and flexural (beam-like) metasurfaces [16,17].

Nonetheless, dispersion curves provide only partial information on the dynamics of a finite system. Evidences of complex phenomena in finite metasurfaces, like lensing [18,19], classical [20] or umklapp [21] mode conversion, rainbow trapping [22] and wave localization [23] are found only from the inspection of the full wave fields. In general, the computation of the wave fields is obtained from numerical harmonic or time transient simulations, using tools like FE software. Given the nature of the wave problems, such simulations are always bounded by their computational cost and often limited by the available hardware resources. Analytical strategies are thus desirable to reduce computational efforts. In addition, analytical methods provide robust tools to study how incident waves interact with multiple scattering sources. In fact, they have been frequently used to investigate how plane waves interact with building-like structures exploiting, for example, series expansion [24], space–frequency mode-matching [25], and homogenization techniques [26–28].

Within this context, in a recent work [29] we proposed a multiple scattering formulation to model Rayleigh waves interacting with a finite length metasurface placed atop an elastic half-space. The considered metasurface comprised an arbitrary number of discrete mass-spring resonators, oscillating along their vertical direction (compressional resonance). In this work we extend the previous formulation by considering flexural-type resonators, namely thin Kirchhoff plates, coupled to the half-space. The formulation is able to account for an arbitrary number N of thin plates. We focus on the low-frequency regime where the flexural contribution of the plates dominates the dynamic response. Thus, we neglect the plates axial behaviour, and the related axial resonances which generally occur at a much higher frequency with respect to the first bending modes.

The key point of our formulation is the solution of the Lamb's problem in terms of Green's functions. Such Green's functions are used to model the incident wave field, due to a known harmonic source acting normally at the surface of the half-space, as well as the scattered wave fields generated by the thin plates when excited by an imposed base displacement. The unknown amplitudes of the N scattered wave fields are found from the solution of the proposed multiple scatting formulation by imposing proper boundary conditions at the half-space surface. The total wave field in the half-space is thus obtained by the coupled contribution of the incident and N scattered wave fields.

Our approach enriches the analytical tools available to discuss the dynamics of flexural metasurfaces, e.g., the closed form dispersion relationships in [16] and the effective models in [27,28], by enabling the description of the finite-size flexural metasurface. To the best of our knowledge, the analytical treatment of this problem remains yet unsolved.

The work is organized as follows. In Section 2, we present the derivation of the theoretical framework. In particular, in Section (a) we begin by recalling the Kirchhoff plate theory to derive the shear and normal stresses at the base of the plates as impedance functions. Then, we recall and use the solution of the Lamb's problem to formulate the incident and scattered wave fields in Section (b). The multiple scattering formulation is finally constructed in Section 3. In Section 4, we investigate and discuss the response of a half-space equipped with a single and a collection of thin plates, and validate our findings via FE simulations. We conclude our work with some remarks and perspectives in Section 5.

2. Theoretical model

We investigate the multiple scattering effects of an array of flexural resonators, namely a flexural metasurface, arranged on the surface of an elastic half-space, as shown in Figure 1. The flexural metasurface can be composed of a series of N parallel thin plates, with different mechanical and geometrical properties. Given the out-of-plane invariance of the configuration, we model the system in the 2D plane described by the spatial coordinates $\boldsymbol{x} = (x, z)$.

The derivation comprises the following three steps: (i) definition of the impedance functions describing the stresses exerted by a thin plate at its base when excited by an imposed base motion; (ii) construction of the half-space Green's functions for such stresses; (iii) formulation of a multiple scattering problem for a half-space coupled with an arbitrary N number of thin plates under a harmonic strip source at the surface.

(a) Impedance boundary conditions of thin plates on an elastic half-space

We model the plates using the Kirchhoff plate theory and their effect on the substrate dynamics using ad-hoc impedance functions. The thin plates are made of homogeneous and linear elastic materials, and are perfectly bonded to the surface of an elastic half-space. We denote the displacement components in the half-space by $u(x, z)$ and $w(x, z)$ along the x and z directions, respectively. The displacement component of the thin plate along the x direction is $U(x, z)$ whereas $\vartheta(x, z) = \partial U(x, z)/\partial z$ denotes the cross-section rotation. For convenience, we introduce a set $\mathcal{B}_n = \{\boldsymbol{x} : x = x_n, 0 \leq z \leq h_n, n \in \mathbb{Z}^+\} \subset \mathbb{R}^2$ to indicate the n-th plate placed at x_n, such that its displacements components read $U_n(z)$ and $\vartheta_n(z)$, for $n = 1, .., N$. We restrict our interest to the harmonic regimes, so that the time-harmonic term $\mathrm{e}^{\mathrm{i}\omega t}$ is omitted through the whole derivation.

The flexural motion of the n-th plate is governed by the equation:

$$\left(\frac{\partial^4}{\partial z^4} - \beta_n^4\right) U_n = 0, \quad \text{for} \quad \boldsymbol{x} \in \mathcal{B}_n \tag{2.1}$$

where β_n denotes the wave number for flexural waves, namely:

$$\beta_n^4 = \frac{\rho_n l_n}{D_n}\omega^2, \quad \text{where} \quad D_n = \frac{E_n}{1-\nu_n^2}\frac{l_n^3}{12} \tag{2.2}$$

in which ρ_n is the material density, l_n is the plate thickness, D_n is the flexural rigidity, E_n is the Young modulus, and ν_n is the Poisson ratio. The general solution of (2.1) has the following form:

$$U_n(z) = C_{n1}\cosh(\beta_n z) + C_{n2}\sinh(\beta_n z) + C_{n3}\cos(\beta_n z) + C_{n4}\sin(\beta_n z). \tag{2.3}$$

in which the four coefficients C_{ni} $(i = 1, 2, 3, 4)$ can be determined by imposing the four boundary conditions (BCs) for flexural vibrations:

$$U_n(0) = u(x_n, 0), \quad \vartheta_n(0) = -\theta(x_n, 0). \tag{2.4a}$$

$$\frac{\partial^2 U_n}{\partial z^2}\Big|_{z=h_n} = 0, \quad \frac{\partial^3 U_n}{\partial z^3}\Big|_{z=h_n} = 0. \tag{2.4b}$$

where the slope of the free surface $\theta(x_n, 0)$ can be expressed in terms of the vertical displacement in the soil w as $\frac{\partial w(x,0)}{\partial x}\Big|_{x=x_n}$.

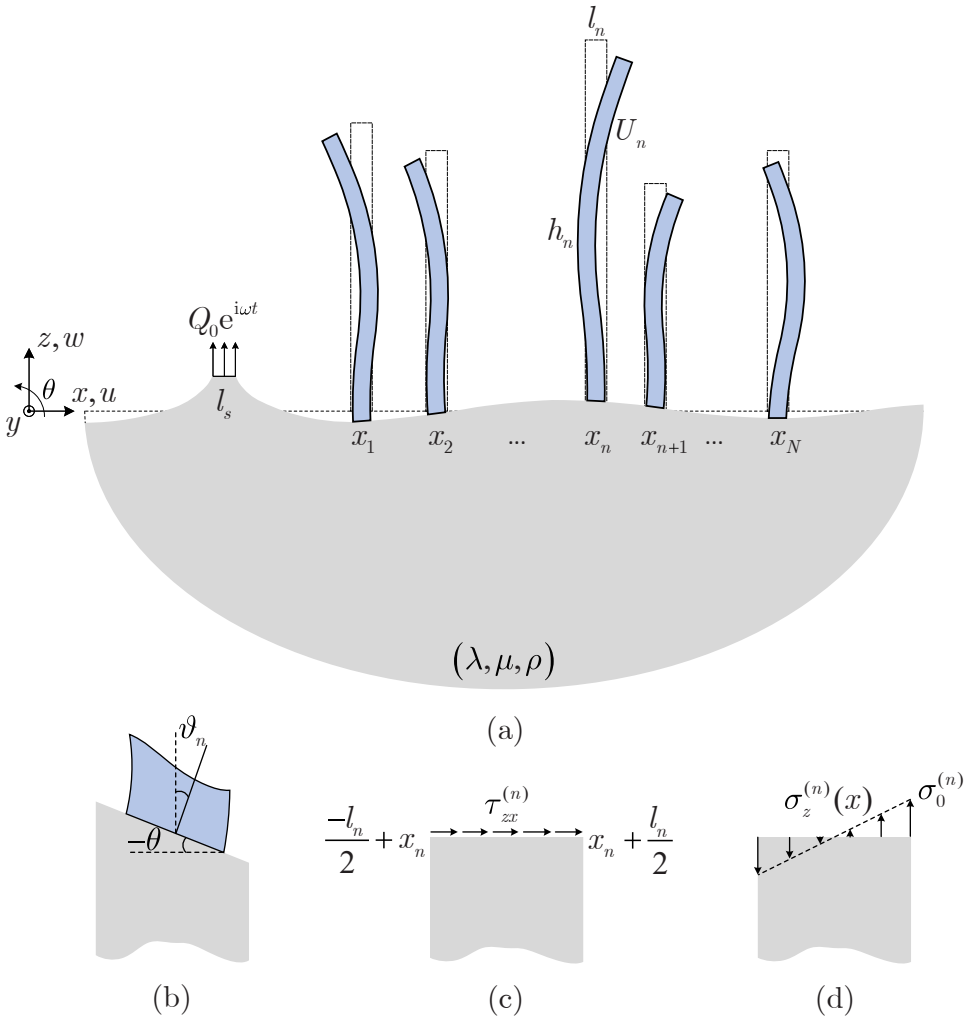

Figure 1. Schematic of elastic waves interacting with a metasurface. (a) An array of arbitrary N thin plates on an elastic half-space, in which h_n and l_n denote the height and thickness of the n-th plate, respectively. (b) Illustration of the continuity of displacements and slope at the plate-substrate interface. The assumed shear and normal stresses caused by the flexural motion of the n-th plate are shown in (c) and (d), respectively.

Equation (2.4*a*) imposes the continuity of displacement and slope at the interface between the n-th plate and the half-space, while (2.4*b*) implies null bending moment and shear force at the plate free end. Expressing (2.4*a*) and (2.4*b*) in terms of (2.3) leads to the following non-homogeneous system:

$$\begin{bmatrix} 1 & 0 & 1 & 0 \\ 0 & 1 & 0 & 1 \\ \cosh(\beta_n h_n) & \sinh(\beta_n h_n) & -\cos(\beta_n h_n) & -\sin(\beta_n h_n) \\ \sinh(\beta_n h_n) & \cosh(\beta_n h_n) & \sin(\beta_n h_n) & -\cos(\beta_n h_n) \end{bmatrix} \begin{bmatrix} C_{n1} \\ C_{n2} \\ C_{n3} \\ C_{n4} \end{bmatrix} = \begin{bmatrix} u(x_n, 0) \\ -\theta(x_n, 0)/\beta_n \\ 0 \\ 0 \end{bmatrix} \tag{2.5}$$

which can be solved for the four unknowns C_{ni}:

$$\begin{aligned} C_{n1} =& \frac{1+\cosh(\beta_n h_n)\cos(\beta_n h_n)+\sinh(\beta_n h_n)\sin(\beta_n h_n)}{2+2\cosh(\beta_n h_n)\cos(\beta_n h_n)} u(x_n,0) \\ & - \frac{\cosh(\beta_n h_n)\sin(\beta_n h_n)-\sinh(\beta_n h_n)\cos(\beta_n h_n)}{2+2\cosh(\beta_n h_n)\cos(\beta_n h_n)} \frac{\theta(x_n,0)}{\beta_n}, \end{aligned} \tag{2.6a}$$

$$\begin{aligned} C_{n2} =& -\frac{\cosh(\beta_n h_n)\sin(\beta_n h_n)+\sinh(\beta_n h_n)\cos(\beta_n h_n)}{2+2\cosh(\beta_n h_n)\cos(\beta_n h_n)} u(x_n,0) \\ & - \frac{1+\cosh(\beta_n h_n)\cos(\beta_n h_n)-\sinh(\beta_n h_n)\sin(\beta_n h_n)}{2+2\cosh(\beta_n h_n)\cos(\beta_n h_n)} \frac{\theta(x_n,0)}{\beta_n}, \end{aligned} \tag{2.6b}$$

$$\begin{aligned} C_{n3} =& \frac{1+\cosh(\beta_n h_n)\cos(\beta_n h_n)-\sinh(\beta_n h_n)\sin(\beta_n h_n)}{2+2\cosh(\beta_n h_n)\cos(\beta_n h_n)} u(x_n,0) \\ & - \frac{\sinh(\beta_n h_n)\cos(\beta_n h_n)-\cosh(\beta_n h_n)\sin(\beta_n h_n)}{2+2\cosh(\beta_n h_n)\cos(\beta_n h_n)} \frac{\theta(x_n,0)}{\beta_n}, \end{aligned} \tag{2.6c}$$

$$\begin{aligned} C_{n4} =& \frac{\cosh(\beta_n h_n)\sin(\beta_n h_n)+\sinh(\beta_n h_n)\cos(\beta_n h_n)}{2+2\cosh(\beta_n h_n)\cos(\beta_n h_n)} u(x_n,0) \\ & - \frac{1+\cosh(\beta_n h_n)\cos(\beta_n h_n)+\sinh(\beta_n h_n)\sin(\beta_n h_n)}{2+2\cosh(\beta_n h_n)\cos(\beta_n h_n)} \frac{\theta(x_n,0)}{\beta_n}. \end{aligned} \tag{2.6d}$$

Given the displacement $U_n(z)$, the shear and normal stresses on the contact area of the n-th plate, i.e. in the region $x \in (x_n - l_n/2, x_n + l_n/2)$ and $z = 0$, can be approximated as (see Figures 1c and 1d):

$$\begin{aligned} \tau_{zx}^{(n)}(x,0) =& -\frac{D_n}{l_n}\frac{\partial^3 U_n}{\partial z^3} = \frac{D_n}{l_n}\beta_n^3(C_4 - C_2) \\ =& \Omega_1^{(n)} u(x_n,0) - \Omega_2^{(n)}\theta(x_n,0), \end{aligned} \tag{2.7a}$$

$$\begin{aligned} \sigma_z^{(n)}(x,0) =& -\frac{E_n}{(1-\nu_n^2)}\frac{\partial^2 U_n}{\partial z^2}(x - x_n) = \frac{E_n}{(1-\nu_n^2)}\beta_n^2(C_3 - C_1)(x - x_n) \\ =& [\Omega_3^{(n)} u(x_n,0) - \Omega_4^{(n)}\theta(x_n,0)](x - x_n). \end{aligned} \tag{2.7b}$$

where the following parameters have been defined:

$$\Omega_1^{(n)} = \frac{D_n}{l_n}\beta_n^3 f_1(\beta_n h_n), \tag{2.8a}$$

$$\Omega_2^{(n)} = \frac{D_n}{l_n}\beta_n^2 f_2(\beta_n h_n), \tag{2.8b}$$

$$\Omega_3^{(n)} = -\frac{E_n}{1-\nu_n^2}\beta_n^2 f_3(\beta_n h_n), \tag{2.8c}$$

$$\Omega_4^{(n)} = -\frac{E_n}{1-\nu_n^2}\beta_n f_4(\beta_n h_n). \tag{2.8d}$$

with:

$$f_1(\beta_n h_n) = \frac{\cosh(\beta_n h_n)\sin(\beta_n h_n)+\sinh(\beta_n h_n)\cos(\beta_n h_n)}{1+\cosh(\beta_n h_n)\cos(\beta_n h_n)}, \tag{2.9a}$$

$$f_2(\beta_n h_n) = f_3(\beta_n h_n) = \frac{\sinh(\beta_n h_n)\sin(\beta_n h_n)}{1+\cosh(\beta_n h_n)\cos(\beta_n h_n)}, \tag{2.9b}$$

$$f_4(\beta_n h_n) = \frac{\cosh(\beta_n h_n)\sin(\beta_n h_n)-\sinh(\beta_n h_n)\cos(\beta_n h_n)}{1+\cosh(\beta_n h_n)\cos(\beta_n h_n)}. \tag{2.9c}$$

In short, equations (2.7*a*) and (2.7*b*) provide the shear and normal stresses at the base of the n-th plate for a given imposed harmonic motion at its base.

Since the system considers an arbitrary number N of plates, the total wave field must be determined considering the incident wave field actuated by the given source plus the contributions of the N scattered wave fields generated by the plates. In what follows, we set a multiple scattering problem, exploiting the Green's function of the Lamb's problem for the incident and scattered waves, and solve it to find the unknown amplitudes of the N scattered wave fields. We show that such amplitudes can be determined by imposing continuity conditions between the impedance functions of the plates, derived above, and the half-space.

(b) Green's functions

Let us briefly recall the fundamental steps of the Lamb's problem [30] to provide the Green's functions in terms of displacement components ($\boldsymbol{u} = [u, w]$), for given time-harmonic shear and normal stress distributions, $\tau_{zx}^{(s)}$ and $\sigma_z^{(s)}$ respectively, acting at the top surface ($z = 0$) of the half-space. This problem can be well defined as a boundary value problem as:

$$\nabla \cdot \mathbb{C} : \nabla \boldsymbol{u} = \rho \ddot{\boldsymbol{u}}, \quad \text{for } z < 0 \tag{2.10a}$$

$$(\mathbb{C} : \nabla \boldsymbol{u}) \cdot \boldsymbol{n} = \left[\sigma_z^{(s)}, \tau_{zx}^{(s)}\right]^T, \quad \text{for } z = 0 \tag{2.10b}$$

where $\mathbb{C}$ and $\boldsymbol{n}$ denote the elastic tensor and the unit normal vector, respectively.

At first, we use the potentials $\varphi(x, z)$, $\psi_y(x, z)$ to decouple the governing equation (2.10*a*) via Helmholtz decomposition [31]:

$$(\nabla^2 + k_p^2)\varphi = 0, \quad (\nabla^2 + k_s^2)\psi_y = 0. \tag{2.11}$$

in which $k_p = \frac{\omega}{c_p}$ and $k_s = \frac{\omega}{c_s}$ denote the wave numbers for compression and shear waves in the half-space, respectively, and where:

$$c_p = \sqrt{\frac{\lambda + 2\mu}{\rho}}, \quad c_s = \sqrt{\frac{\mu}{\rho}}. \tag{2.12}$$

are the compression and shear wave velocities, respectively, being λ and μ the Lamé constants and ρ the mass density of the half-space.

Making use of the spatial Fourier transform pairs:

$$\bar{f}(k, z) = \int_{-\infty}^{\infty} f(x, z) \mathrm{e}^{-\mathrm{i}kx} \, \mathrm{d}x, \quad f(x, z) = \frac{1}{2\pi} \int_{-\infty}^{\infty} \bar{f}(k, z) \mathrm{e}^{\mathrm{i}kx} \, \mathrm{d}k. \tag{2.13}$$

we obtain the transformed wave equations (2.11) as:

$$\left(\frac{\partial^2}{\partial z^2} - p^2\right) \bar{\varphi} = 0, \quad \left(\frac{\partial^2}{\partial z^2} - q^2\right) \bar{\psi}_y = 0. \tag{2.14}$$

which admit solutions of the form:

$$\bar{\varphi}(k, z) = A_1 \mathrm{e}^{-pz} + B_1 \mathrm{e}^{pz}, \quad \bar{\psi}_y(k, z) = A_2 \mathrm{e}^{-qz} + B_2 \mathrm{e}^{qz}. \tag{2.15}$$

where p and q read:

$$p = \sqrt{k^2 - k_p^2}, \quad q = \sqrt{k^2 - k_s^2}. \tag{2.16}$$

where the coefficients A_1, A_2 must be zero to avoid an unbounded response for $z = -\infty$, while B_1, B_2 are determined by imposing stress BCs at $z = 0$.

To this purpose, we first express the normal and shear stresses in the half-space in terms of the potentials:

$$\sigma_z(x,z) = -\mu\left[k_s^2\varphi + 2\left(\frac{\partial^2\varphi}{\partial x^2} - \frac{\partial^2\psi_y}{\partial x\partial z}\right)\right], \tag{2.17a}$$

$$\tau_{zx}(x,z) = -\mu\left[k_s^2\psi_y - 2\left(\frac{\partial^2\varphi}{\partial x\partial z} - \frac{\partial^2\psi_y}{\partial z^2}\right)\right]. \tag{2.17b}$$

Next, we Fourier transform the stress components in (2.17*a*) and (2.17*b*) and impose their values at $z = 0$ equal to those given by the boundary condition in (2.10*b*) as:

$$\bar{\sigma}_z(k,0) = \mu[(2k^2 - k_s^2)B_1 + 2\mathrm{i}kqB_2] = \bar{\sigma}_z^{(s)}(k,0), \tag{2.18a}$$

$$\bar{\tau}_{zx}(k,0) = \mu[2\mathrm{i}kpB_1 - (2k^2 - k_s^2)B_2] = \bar{\tau}_{zx}^{(s)}(k,0), \tag{2.18b}$$

where the superscript (s) denotes the stresses generated by the source function. Solving (2.18*a*) and (2.18*b*) yields the coefficients:

$$B_1 = \frac{(2\mathrm{i}kq)\bar{\tau}_{zx}^{(s)}(k,0) + (2k^2 - k_s^2)\bar{\sigma}_z^{(s)}(k,0)}{\mu R(k)}, \tag{2.19a}$$

$$B_2 = \frac{-(2k^2 - k_s^2)\bar{\tau}_{zx}^{(s)}(k,0) + (2\mathrm{i}kp)\bar{\sigma}_z^{(s)}(k,0)}{\mu R(k)}, \tag{2.19b}$$

where $R(k)$ is known as the Rayleigh function:

$$R(k) = (2k^2 - k_s^2)^2 - 4k^2pq. \tag{2.20}$$

According to the Helmholtz decomposition, the displacement components in the half-space can be expressed as:

$$u = \frac{\partial\varphi}{\partial x} - \frac{\partial\psi_y}{\partial z}, \quad w = \frac{\partial\varphi}{\partial z} + \frac{\partial\psi_y}{\partial x}. \tag{2.21}$$

Fourier transforming (2.21), and substituting (2.15), (2.19*a*) and (2.19*b*), yield:

$$\begin{aligned}\bar{u}(k,z) &= \mathrm{i}k\bar{\varphi} - \frac{\partial\bar{\psi}_y}{\partial z}\\ &= \frac{-2k^2q\mathrm{e}^{pz} + q(2k^2 - k_s^2)\mathrm{e}^{qz}}{\mu R(k)}\bar{\tau}_{zx}^{(s)}(k,0) + \frac{\mathrm{i}k(2k^2 - k_s^2)\mathrm{e}^{pz} - (2\mathrm{i}kpq)\mathrm{e}^{qz}}{\mu R(k)}\bar{\sigma}_z^{(s)}(k,0),\end{aligned} \tag{2.22a}$$

$$\begin{aligned}\bar{w}(k,z) &= \frac{\partial\bar{\varphi}}{\partial z} + \mathrm{i}k\bar{\psi}_y\\ &= \frac{(2\mathrm{i}kpq)\mathrm{e}^{pz} - \mathrm{i}k(2k^2 - k_s^2)\mathrm{e}^{qz}}{\mu R(k)}\bar{\tau}_{zx}^{(s)}(k,0) + \frac{p(2k^2 - k_s^2)\mathrm{e}^{pz} - 2k^2p\mathrm{e}^{qz}}{\mu R(k)}\bar{\sigma}_z^{(s)}(k,0).\end{aligned} \tag{2.22b}$$

At last, the inverse Fourier transform of (2.22*a*) and (2.22*b*) provides the wave field displacement components due to time-harmonic stresses imposed at the surface as:

$$u(x,z) = \frac{1}{2\pi\mu}\int_{-\infty}^{\infty}\left[\frac{-2k^2q\mathrm{e}^{pz} + q(2k^2 - k_s^2)\mathrm{e}^{qz}}{R(k)}\bar{\tau}_{zx}^{(s)}(k,0) + \frac{\mathrm{i}k(2k^2 - k_s^2)\mathrm{e}^{pz} - (2\mathrm{i}kpq)\mathrm{e}^{qz}}{R(k)}\bar{\sigma}_z^{(s)}(k,0)\right]\mathrm{e}^{\mathrm{i}kx}\,\mathrm{d}k, \tag{2.23a}$$

$$w(x,z) = \frac{1}{2\pi\mu}\int_{-\infty}^{\infty}\left[\frac{(2\mathrm{i}kpq)\mathrm{e}^{pz} - \mathrm{i}k(2k^2 - k_s^2)\mathrm{e}^{qz}}{R(k)}\bar{\tau}_{zx}^{(s)}(k,0) + \frac{p(2k^2 - k_s^2)\mathrm{e}^{pz} - 2k^2p\mathrm{e}^{qz}}{R(k)}\bar{\sigma}_z^{(s)}(k,0)\right]\mathrm{e}^{\mathrm{i}kx}\,\mathrm{d}k. \tag{2.23b}$$

In what follows, we specialize these Green's functions for the stress distributions considered in this work, namely (i) a uniform normal stress distribution, used to model the external

source (see Figure 1a), and (ii) a constant shear stress distribution and (iii) a butterfly normal stress distribution, as shown in Figure 1c and Figure 1d, respectively, used to model the stress components generated by the flexural motion of the plates.

(i) Uniform normal stress distribution to model the source

We consider a vertically distributed source with footprint width l_s centred at the origin of the reference system, as shown in Figure 1a. The BCs on the free surface ($z=0$) are:

$$\sigma_z(x,0) = \begin{cases} Q_0 & \text{if } |x| \le l_s/2 \\ 0 & \text{elsewhere} \end{cases}, \qquad \tau_{zx}(x,0) = 0, \tag{2.24}$$

where Q_0 is the magnitude of the source. Fourier transforming (2.24) yields:

$$\bar{\sigma}_z(k,0) = \frac{2Q_0}{k}\sin(kl_s/2), \quad \bar{\tau}_{zx}(k,0) = 0. \tag{2.25}$$

Substituting (2.25) into (2.23*a*) and (2.23*b*) we can obtain the displacement components due to a unitary normal stress ($Q_0 = 1$ Pa) acting at the free surface, namely the Green's functions:

$$G_{\sigma u}(x,z) = \frac{\mathrm{i}}{\pi\mu}\int_{-\infty}^{\infty} \sin(kl_s/2)\frac{(2k^2-k_s^2)\mathrm{e}^{pz} - 2pq\mathrm{e}^{qz}}{R(k)}\mathrm{e}^{\mathrm{i}kx}\,\mathrm{d}k, \tag{2.26a}$$

$$G_{\sigma w}(x,z) = \frac{1}{\pi\mu}\int_{-\infty}^{\infty} \frac{\sin(kl_s/2)}{k}\frac{p(2k^2-k_s^2)\mathrm{e}^{pz} - 2k^2p\mathrm{e}^{qz}}{R(k)}\mathrm{e}^{\mathrm{i}kx}\,\mathrm{d}k. \tag{2.26b}$$

Additionally, by deriving (2.26*b*) with respect to the x coordinate, we can obtain the Green's function related to the slope of the half-space:

$$G_{\sigma\theta}(x,z) = \frac{\partial G_{\sigma w}(x,z)}{\partial x} = \frac{\mathrm{i}}{\pi\mu}\int_{-\infty}^{\infty} \sin(kl_s/2)\frac{p(2k^2-k_s^2)\mathrm{e}^{pz} - 2k^2p\mathrm{e}^{qz}}{R(k)}\mathrm{e}^{\mathrm{i}kx}\,\mathrm{d}k. \tag{2.26c}$$

(ii) Uniform shear stress distribution

Following the same approach, we here deduce the Green's functions for a uniform shear stress distribution on the surface, as the one shown in Figure 1c. The BCs on the free surface ($z=0$) are:

$$\sigma_z(x,0) = 0, \quad \tau_{zx}(x,0) = \begin{cases} Q_x^{(n)} & \text{if } |x-x_n| \le l_n/2 \\ 0 & \text{elsewhere} \end{cases}, \tag{2.27}$$

where $Q_x^{(n)}$ is the magnitude of τ_{zx}. Fourier transforming (2.27) yields:

$$\bar{\sigma}_z(k,0) = 0, \quad \bar{\tau}_{zx}(k,0) = \frac{2Q_x^{(n)}}{k}\sin(kl_n/2)\mathrm{e}^{-\mathrm{i}kx_n}. \tag{2.28}$$

Substituting (2.28) into (2.23*a*) and (2.23*b*) leads to the displacement components induced by unitary shear stress ($Q_x^{(n)} = 1$ Pa) applied at the free surface, as:

$$G_{\tau u}^{(n)}(x,z) = \frac{-1}{\pi\mu}\int_{-\infty}^{\infty} \frac{\sin(kl_n/2)}{k}\frac{2k^2q\mathrm{e}^{pz} - q(2k^2-k_s^2)\mathrm{e}^{qz}}{R(k)}\mathrm{e}^{\mathrm{i}k(x-x_n)}\,\mathrm{d}k, \tag{2.29a}$$

$$G_{\tau w}^{(n)}(x,z) = \frac{\mathrm{i}}{\pi\mu}\int_{-\infty}^{\infty} \sin(kl_n/2)\frac{2pq\mathrm{e}^{pz} - (2k^2-k_s^2)\mathrm{e}^{qz}}{R(k)}\mathrm{e}^{\mathrm{i}k(x-x_n)}\,\mathrm{d}k. \tag{2.29b}$$

By deriving (2.29*b*) with respect to the x coordinate, we obtain the Green's function related to the slope of the half-space:

$$G_{\tau\theta}^{(n)}(x,z) = \frac{\partial G_{\tau w}^{(n)}(x,z)}{\partial x} = \frac{-1}{\pi\mu}\int_{-\infty}^{\infty} k\sin(kl_n/2)\frac{2pq\mathrm{e}^{pz} - (2k^2-k_s^2)\mathrm{e}^{qz}}{R(k)}\mathrm{e}^{\mathrm{i}k(x-x_n)}\,\mathrm{d}k. \tag{2.29c}$$

(iii) Butterfly-shaped normal stress distribution

At last, we derive the Green's functions for a butterfly-shaped distribution of normal stress on the surface, as shown in Figure 1d. In this case, the BCs on the free surface ($z=0$) are:

$$\sigma_z(x,0)=\begin{cases} 2\sigma_0^{(n)}(x-x_n)/l_n & \text{if } |x-x_n|\le l_n/2 \\ 0 & \text{elsewhere}\end{cases}, \quad \tau_{zx}(x,0)=0, \tag{2.30}$$

in which $\sigma_0^{(n)}$ is the maximum values of σ_z. Fourier transforming (2.30) yields:

$$\bar{\sigma}_z(k,0)=\frac{4\mathrm{i}\sigma_0^{(n)}}{l_n k^2}\left[\frac{kl_n}{2}\cos(\frac{kl_n}{2})-\sin(\frac{kl_n}{2})\right]\mathrm{e}^{-\mathrm{i}kx_n}, \quad \bar{\tau}_{zx}(k,0)=0. \tag{2.31}$$

By substituting (2.31) into (2.23*a*) and (2.23*b*) we obtain the displacement components induced by a butterfly-shaped normal stress ($\sigma_0^{(n)}=1$ Pa) acting on the free surface:

$$G^{(n)}_{\sigma_0 u}(x,z)=\frac{-2}{\pi\mu l_n}\int_{-\infty}^{\infty}\left[\frac{kl_n}{2}\cos(\frac{kl_n}{2})-\sin(\frac{kl_n}{2})\right]\frac{(2k^2-k_s^2)\mathrm{e}^{pz}-2pq\mathrm{e}^{qz}}{kR(k)}\mathrm{e}^{\mathrm{i}k(x-x_n)}\,\mathrm{d}k, \tag{2.32a}$$

$$G^{(n)}_{\sigma_0 w}(x,z)=\frac{2\mathrm{i}}{\pi\mu l_n}\int_{-\infty}^{\infty}\left[\frac{kl_n}{2}\cos(\frac{kl_n}{2})-\sin(\frac{kl_n}{2})\right]\frac{p(2k^2-k_s^2)\mathrm{e}^{pz}-2k^2p\mathrm{e}^{qz}}{k^2R(k)}\mathrm{e}^{\mathrm{i}k(x-x_n)}\,\mathrm{d}k. \tag{2.32b}$$

Finally, by deriving (2.32*b*) with respect to the x coordinate we obtain:

$$G^{(n)}_{\sigma_0\theta}(x,z)=\frac{\partial G^{(n)}_{\sigma_0 w}(x,z)}{\partial x}=\frac{-2}{\pi\mu l_n}\int_{-\infty}^{\infty}\left[\frac{kl_n}{2}\cos(\frac{kl_n}{2})-\sin(\frac{kl_n}{2})\right]\frac{p(2k^2-k_s^2)\mathrm{e}^{pz}-2k^2p\mathrm{e}^{qz}}{kR(k)}\mathrm{e}^{\mathrm{i}k(x-x_n)}\,\mathrm{d}k. \tag{2.32c}$$

3. Multiple scattering formulation

In this section we develop a multiple scattering formulation to quantitatively model the destructive or constructive interference between the waves generated by a harmonic distributed source, acting at the surface, and those actuated by the flexural motion of the N plates. Our scope is to calculate the amplitude of the tangential and normal stresses at the base of each plate. Once these stresses are known, the total wave field can be obtained by the superposition of the incident and scattered waves computed using the Green's functions introduced in Section 2b.

For convenience, we define a set $\mathcal{O}=\{\boldsymbol{x}: x=x_m, z=0, m=1,...,N\}\subset\mathbb{R}^2$ to collect the plate locations. When the incident field impinges on the array of N plates, the total wavefield can be expressed as the summation of incident and scattered fields:

$$u(x,z)=u_0(x,z)+\sum_{n=1}^{N}Q_x^{(n)}G^{(n)}_{\tau u}(x,z)+\sum_{n=1}^{N}\sigma_0^{(n)}G^{(n)}_{\sigma_0 u}(x,z), \tag{3.1a}$$

$$w(x,z)=w_0(x,z)+\sum_{n=1}^{N}Q_x^{(n)}G^{(n)}_{\tau w}(x,z)+\sum_{n=1}^{N}\sigma_0^{(n)}G^{(n)}_{\sigma_0 w}(x,z), \tag{3.1b}$$

$$\theta(x,z)=\theta_0(x,z)+\sum_{n=1}^{N}Q_x^{(n)}G^{(n)}_{\tau\theta}(x,z)+\sum_{n=1}^{N}\sigma_0^{(n)}G^{(n)}_{\sigma_0\theta}(x,z), \tag{3.1c}$$

where u_0, w_0 and θ_0 denote, respectively, the displacement components and rotation in the half-space due to the incident wavefield as follows:

$$u_0(x,z)=Q_0G_{\sigma u}(x,z), \tag{3.2a}$$

$$w_0(x,z)=Q_0G_{\sigma w}(x,z), \tag{3.2b}$$

$$\theta_0(x,z)=Q_0G_{\sigma\theta}(x,z). \tag{3.2c}$$

We substitute equations (3.2*a*, 3.2*c*) into (3.1*a*) and (3.1*c*) and specify them at the plate location x_m:

$$u(x_m,0) = Q_0 G_{\sigma u}(x_m,0) + \sum_{n=1}^{N} Q_x^{(n)} G_{\tau u}^{(n)}(x_m,0) + \sum_{n=1}^{N} \sigma_0^{(n)} G_{\sigma_0 u}^{(n)}(x_m,0), \tag{3.3a}$$

$$\theta(x_m,0) = Q_0 G_{\sigma\theta}(x_m,0) + \sum_{n=1}^{N} Q_x^{(n)} G_{\tau\theta}^{(n)}(x_m,0) + \sum_{n=1}^{N} \sigma_0^{(n)} G_{\sigma_0\theta}^{(n)}(x_m,0). \tag{3.3b}$$

Similarly, we consider the shear and normal stresses at the base of the plate, i.e., (2.7*a*) and (2.7*b*), respectively, and express them in force of (2.27) and (2.30):

$$Q_x^{(m)} = \Omega_1^{(m)} u(x_m,0) - \Omega_2^{(m)} \theta(x_m,0), \tag{3.4a}$$

$$2\sigma_0^{(m)}/l_m = \Omega_3^{(m)} u(x_m,0) - \Omega_4^{(m)} \theta(x_m,0). \tag{3.4b}$$

At this stage, we can express the displacements $u(x_m,0)$ and $\theta(x_m,0)$ in (3.4*a*) and (3.4*b*) by means of (3.3*a*) and (3.3*b*) to obtain:

$$\begin{aligned} Q_x^{(m)} = {} & Q_0 \left[\Omega_1^{(m)} G_{\sigma u}(x_m,0) - \Omega_2^{(m)} G_{\sigma\theta}(x_m,0)\right] \\ & + \sum_{n=1}^{N} Q_x^{(n)} \left[\Omega_1^{(m)} G_{\tau u}^{(n)}(x_m,0) - \Omega_2^{(m)} G_{\tau\theta}^{(n)}(x_m,0)\right] \\ & + \sum_{n=1}^{N} \sigma_0^{(n)} \left[\Omega_1^{(m)} G_{\sigma_0 u}^{(n)}(x_m,0) - \Omega_2^{(m)} G_{\sigma_0\theta}^{(n)}(x_m,0)\right], \end{aligned} \tag{3.5a}$$

$$\begin{aligned} 2\sigma_0^{(m)}/l_m = {} & Q_0 \left[\Omega_3^{(m)} G_{\sigma u}(x_m,0) - \Omega_4^{(m)} G_{\sigma\theta}(x_m,0)\right] \\ & + \sum_{n=1}^{N} Q_x^{(n)} \left[\Omega_3^{(m)} G_{\tau u}^{(n)}(x_m,0) - \Omega_4^{(m)} G_{\tau\theta}^{(n)}(x_m,0)\right] \\ & + \sum_{n=1}^{N} \sigma_0^{(n)} \left[\Omega_3^{(m)} G_{\sigma_0 u}^{(n)}(x_m,0) - \Omega_4^{(m)} G_{\sigma_0\theta}^{(n)}(x_m,0)\right]. \end{aligned} \tag{3.5b}$$

With some algebra, equations (3.5*a*) and (3.5*b*) can be reorganized as:

$$\begin{aligned} -Q_0 \left[\Omega_1^{(m)} G_{\sigma u}(x_m,0) - \Omega_2^{(m)} G_{\sigma\theta}(x_m,0)\right] = {} & \sum_{n=1}^{N} Q_x^{(n)} \left[\Omega_1^{(m)} G_{\tau u}^{(n)}(x_m,0) - \Omega_2^{(m)} G_{\tau\theta}^{(n)}(x_m,0) - \delta_n^m\right] \\ & + \sum_{n=1}^{N} \sigma_0^{(n)} \left[\Omega_1^{(m)} G_{\sigma_0 u}^{(n)}(x_m,0) - \Omega_2^{(m)} G_{\sigma_0\theta}^{(n)}(x_m,0)\right], \end{aligned} \tag{3.6a}$$

$$\begin{aligned} -Q_0 \left[\Omega_3^{(m)} G_{\sigma u}(x_m,0) - \Omega_4^{(m)} G_{\sigma\theta}(x_m,0)\right] = {} & \sum_{n=1}^{N} Q_x^{(n)} \left[\Omega_3^{(m)} G_{\tau u}^{(n)}(x_m,0) - \Omega_4^{(m)} G_{\tau\theta}^{(n)}(x_m,0)\right] \\ & + \sum_{n=1}^{N} \sigma_0^{(n)} \left[\Omega_3^{(m)} G_{\sigma_0 u}^{(n)}(x_m,0) - \Omega_4^{(m)} G_{\sigma_0\theta}^{(n)}(x_m,0) - 2\delta_n^m/l_n\right]. \end{aligned} \tag{3.6b}$$

where δ_n^m is the Kronecker delta.

Equations (3.6*a*) and (3.6*b*), applied to $\boldsymbol{x} \in \mathcal{O}$, provide a system of $2 \times N$ non homogeneous linear equations, in the $2 \times N$ unknown coefficients $Q_x^{(n)}$ and $\sigma_0^{(n)}$, written in compact form as:

$$\boldsymbol{S}\boldsymbol{y} = \boldsymbol{b}, \tag{3.7}$$

in which the corresponding coefficients are:

$$\boldsymbol{S} = \begin{bmatrix} \boldsymbol{S}_{11} & \boldsymbol{S}_{12} \\ \boldsymbol{S}_{21} & \boldsymbol{S}_{22} \end{bmatrix}, \quad \boldsymbol{y} = \begin{bmatrix} Q_x^{(n)} \\ \sigma_0^{(n)} \end{bmatrix}, \quad \boldsymbol{b} = \begin{bmatrix} \boldsymbol{b}_1 \\ \boldsymbol{b}_2 \end{bmatrix}, \tag{3.8}$$

with components:

$$\boldsymbol{S}_{11} = \sum_{n=1}^{N} \left[\Omega_1^{(m)} G_{\tau u}^{(n)}(x_m, 0) - \Omega_2^{(m)} G_{\tau\theta}^{(n)}(x_m, 0) - \delta_n^m \right], \tag{3.9a}$$

$$\boldsymbol{S}_{12} = \sum_{n=1}^{N} \left[\Omega_1^{(m)} G_{\sigma_0 u}^{(n)}(x_m, 0) - \Omega_2^{(m)} G_{\sigma_0\theta}^{(n)}(x_m, 0) \right], \tag{3.9b}$$

$$\boldsymbol{S}_{21} = \sum_{n=1}^{N} \left[\Omega_3^{(m)} G_{\tau u}^{(n)}(x_m, 0) - \Omega_4^{(m)} G_{\tau\theta}^{(n)}(x_m, 0) \right], \tag{3.9c}$$

$$\boldsymbol{S}_{22} = \sum_{n=1}^{N} \left[\Omega_3^{(m)} G_{\sigma_0 u}^{(n)}(x_m, 0) - \Omega_4^{(m)} G_{\sigma_0\theta}^{(n)}(x_m, 0) - 2\delta_n^m / l_n \right], \tag{3.9d}$$

$$\boldsymbol{b}_1 = -Q_0 \left[\Omega_1^{(m)} G_{\sigma u}(x_m, 0) - \Omega_2^{(m)} G_{\sigma\theta}(x_m, 0) \right], \tag{3.9e}$$

$$\boldsymbol{b}_2 = -Q_0 \left[\Omega_3^{(m)} G_{\sigma u}(x_m, 0) - \Omega_4^{(m)} G_{\sigma\theta}(x_m, 0) \right]. \tag{3.9f}$$

To avoid numerical instabilities in the solution of (3.7), we assume a small hysteretic damping ratio $\zeta = 0.1\%$ in both the substrate and the plates elastic response to remove the poles at $k = \pm k_r$ of the integrands in the Green's functions, where $\pm k_r$ are the roots of the Rayleigh function in (2.20). As such, the Lamé constants in integrands are replaced by the complex moduli as $\lambda' = \lambda(1 + 2\mathrm{i}\zeta)$ and $\mu' = \mu(1 + 2\mathrm{i}\zeta)$ [32]. Additionally, the Green's functions are evaluated via the Gauss-Kronrod quadrature formula by a truncated integration as $\int_{-k_\ell}^{+k_\ell}(\cdot)\,\mathrm{d}k$, where k_ℓ is a truncated upper limit [33,34]. Due to the oscillating nature of the integrand, the integration rapidly converges when $k_\ell \gg k_r$.

The computed coefficients $Q_x^{(n)}$ and $\sigma_0^{(n)}$ are finally used into (3.1*a*) and (3.1*b*) to obtain the total wavefield in the half-space.

4. Numerical examples

In this section, we assess the validity of the proposed multiple scattering formulation, namely (3.1*a*, 3.1*b*) by modelling three case studies. The first case considers the interaction of Rayleigh waves with a single plate; in the second example, we model the interaction between five distinct plates arranged in a random configuration; the last scenario describes the response of a finite-size metasurface composed of 30 plates. The mechanical and geometrical parameters of the three examples are collected in Table 1.

Before delving into the description of the case studies, let us discuss the impedance properties derived in (2.8*a*-2.8*d*) which depend on the dimensionless functions f_i $(i = 1, ..., 4)$. The variations of these dimensionless functions with respect to the frequency are reported in Figure 2, where the dimensionless frequency $\bar{\omega} = \omega l/(\pi c_s)$ is used [31]. According to (2.7*a*), the shear stress provided by the plate flexural motion is determined by both f_1 and f_2, here collected in Figure 2a. In the frequency range $\bar{\omega} = [0, 0.18]$ the impedance parameters f_1 and f_2 present six identical resonance peaks, which correspond to the first six flexural resonances of a cantilever plate, i.e., $1 + \cosh(\beta h)\cos(\beta h) = 0$. Strong interaction effects between the plate and the half-space dynamics are expected in the vicinity of these flexural resonances, while minimal coupling occurs

Table 1. Mechanical parameters for plates and the elastic half-space [16].

Symbol	Definition	Value
Q_0	Distributed source amplitude	1 MPa
l_s	Footprint thickness of the source	1 m
ρ	Mass density of half-space	13000 kg/m^3
λ	First Lamé constant of half-space	702 MPa
μ	Shear modulus of half-space	325 MPa
l_n	Plate thickness	0.3 m
ρ_n	Plate density	450 kg/m^3
E_n	Young modulus of plate	1547 MPa
ν_n	Poisson ratio of plate	0.3
ζ	Hysteretic damping ratio	0.1%

at the valley points. It should be noted that the minimum values of f_1 and f_2 do not overlap except for the static condition (zero frequency), suggesting that the flexural motion of the plate always exchange non-zero shear stresses with the surface half-space. The same arguments apply to the dimensionless impedance functions f_3 and f_4, reported in Figure 2b, which govern the normal stress exerted by the plate on the half-space.

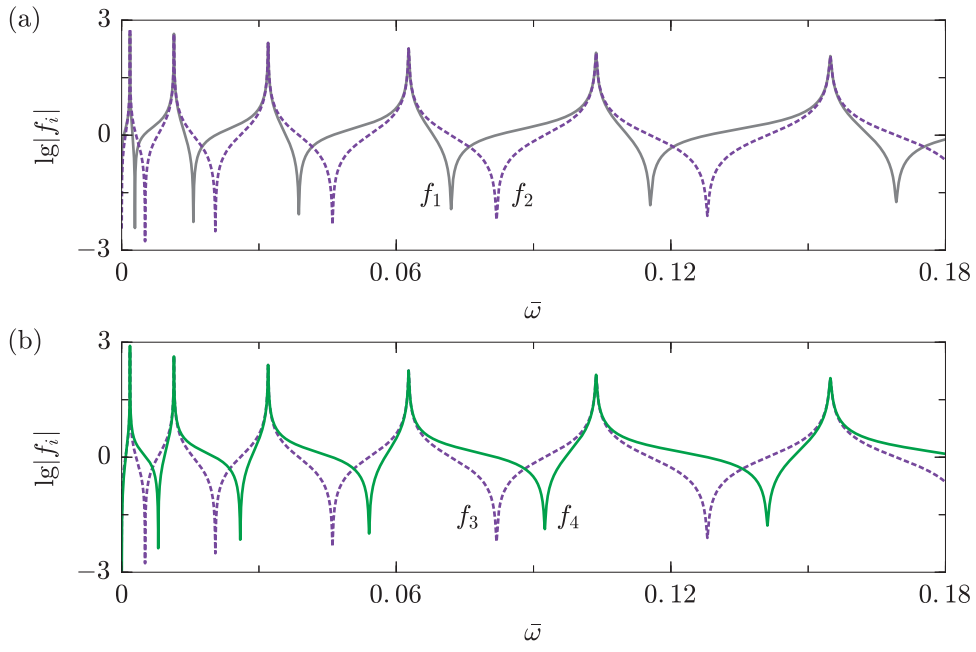

Figure 2. Variations of the impedance parameters vs. frequency ($l = 0.3$ m and $h = 14$ m).

(a) Single plate scenario

A thin plate with $l_1 = 0.3$ m and $h_1 = 14$ m is located at $x_1 = 100$ m, $z = 0$ m and is excited by a harmonic distributed source with footprint thickness $l_s = 1$ m and amplitude $Q_0 = 1$ MPa located at the origin of the coordinate system. To evaluate the interaction between Rayleigh waves and

flexural motions of plates, we introduce the amplitude ratio on the half-space surface ($z = 0$) as [35]:

$$A_R = |u/u_0|. \tag{4.1}$$

Figure 3a shows the A_R at $x = 120\,\mathrm{m}$, $z = 0\,\mathrm{m}$ for $\bar{\omega} \in [0, 0.18]$ which includes the first six flexural resonances.

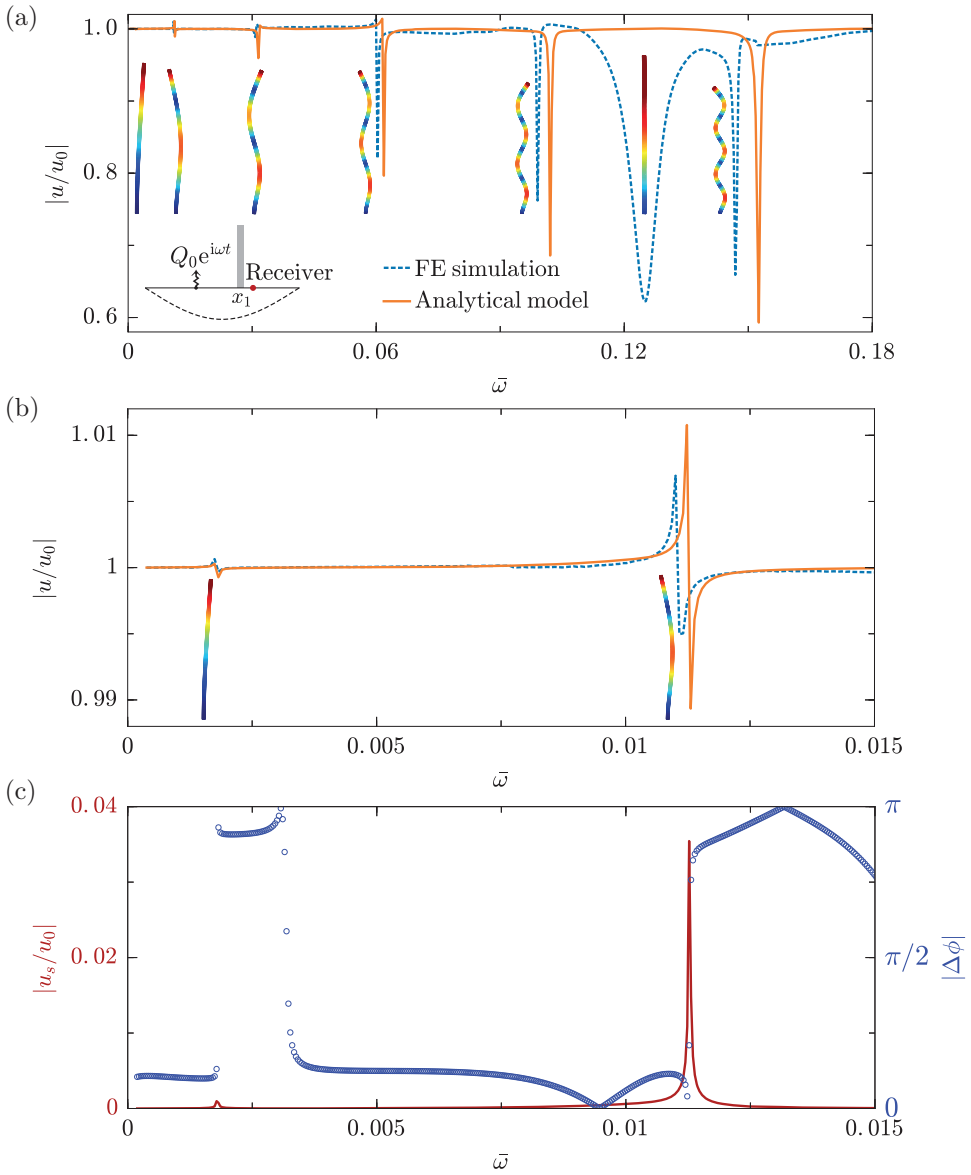

Figure 3. (a) Amplitude ratio $A_R = |u/u_0|$ of a single plate ($l_1 = 0.3\,\mathrm{m}$ and $h_1 = 14\,\mathrm{m}$). The plate is located at $x_1 = 100\,\mathrm{m}$ and the receiver $x = 120\,\mathrm{m}$. (b) Zoomed-in amplitude ratio in the low-frequency regime. (c) Spectrum and phase of the scattered field vs. the free field, denoted by the solid line and circles, respectively.

For comparison, we provide the same amplitude ratio computed via a 2D FE simulation (dashed line). In the FE environment, both the plate and the half-space are modelled using 2D

plane strain elasticity (see the supplementary material for details on the model). Nonetheless, a very good agreement between the results obtained by using the proposed formulation and the FE is found. One can observe that the interaction between the plate and the half-space in the vicinity of the plate resonances yields minimal values of the amplitude ratio. The drops in the low-frequency range can be better appreciated in Figure 3b, where the amplitude ratio is shown in the frequency range $\bar{\omega} \in [0, 0.015]$.

To better understand the A_R, we expand the expression as:

$$A_R = \left|1 + \frac{u_s}{u_0}\right| = \sqrt{1 + \left|\frac{u_s}{u_0}\right|^2 + 2\left|\frac{u_s}{u_0}\right| \cos(\Delta\phi)}, \tag{4.2}$$

where $\Delta\phi$ is the relative phase between the scattered and incident horizontal displacements, namely, u_s/u_0. Equation (4.2) indicates that the A_R is determined by both the amplitude and relative phase of scattered wave fields. The scattered field reaches its peak at the resonance frequencies of the plate, accompanied by a phase shift about 180 degrees (see Figure 3c), which results in the peaks/drops of the amplitude ratio in Figure 3b.

Note that the flexural resonances computed by the analytical model occur at frequency values slightly higher than the actual 2D FE results. Indeed, our formulation based on the Kirchhoff plate theory neglects both the shear deformation and rotary inertia, making the model more rigid than the 2D plane strain model. Besides, we remind that the proposed formulation does not capture the axial resonance of the plate, i.e. the valley between the fifth and sixth bending resonance, since we consider the flexural motion of the plate only. The reader can appreciate the nature of the different resonant modes from the modal shapes provided in the figure inset.

Additionally, let us remark that the proposed formulation reduces significantly the computational cost needed to obtain the amplitude ratio, as it can compute the output at the desired receiver location without the need for a discretization of the whole model, as in the case of FE models. For example, with a personal computer, it takes only a few seconds to simulate the system in Figure 3 while around one hour for the FE model. Finally, we remark that the proposed methodology is capable of discussing the mass-loading effect. The reader can appreciate the details in the supplementary material.

(b) Randomly distributed plates

As a second example, we consider a system of five different plates arranged atop the half-space in the arbitrary configuration shown in the inset of Figure 4. Random arrangements of flexural resonators are often found in urban vibration problems, i.e., where a series of buildings are impacted by seismic waves and their responses are affected by those of the other buildings, also known as building-soil-building interactions [24,25]. We show that an arbitrary configuration of flexural resonators can be readily modelled by our formulation.

The five plates are characterized by the following geometrical parameters: $l = [0.3, 0.2, 0.6, 0.4, 0.5]$ m, $h = [14, 10, 16, 12, 10]$ m, and location $x = [100, 102, 106, 116, 118]$ m. The fundamental resonance frequencies of the five plates atop the half-space are [0.47, 0.61, 0.7, 0.83, 1.48] Hz. The amplitude ratio at $x = 130$ m, $z = 0$ m for $\bar{\omega} \in [0, 0.085]$, as calculated by our formulation, is shown in Figure 4 (solid line). As for the single plate scenario, the interaction between the plates resonances and the substrate wave field results in multiple drops of the amplitude ratio, located at the plate resonances. For comparison, we also provide the results of a FE simulation (dashed line), developed using 2D plane-strain elasticity model, which well agree with those of the analytical framework.

Finally, in Figure 5 we show the horizontal response of the top of the first plate, i.e., $U_1(h_1)$, calculated using our formulation (solid line). In particular, the response at the top of the plate is found via equation (2.3) once the base displacement and rotation, namely $u(x_1, 0)$ and $\theta(x_1, 0)$, are computed. It can be observed that the four peaks in the spectrum match perfectly with the first four resonances of the plate (see Figure 3). Additionally, we still observe some small valleys

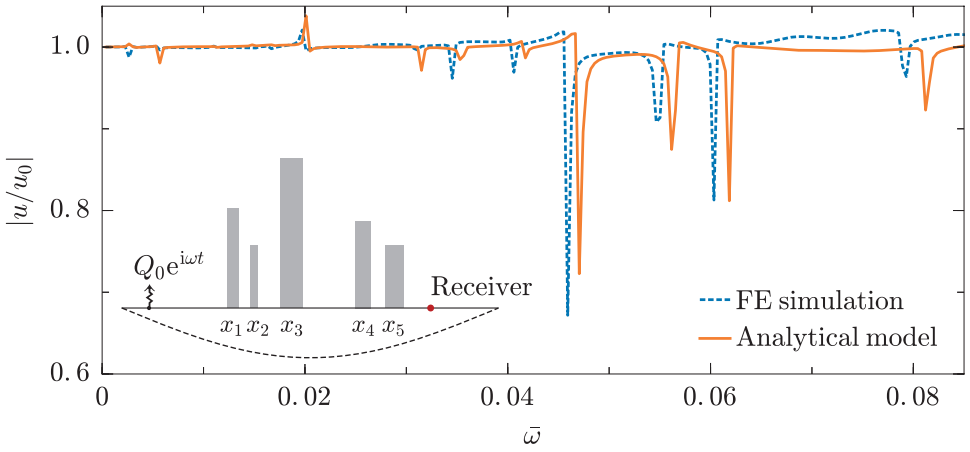

Figure 4. Amplitude ratio $A_R = |u/u_0|$ for a configuration of five randomly distributed plates. The receiver is located at $x = 130\,\mathrm{m}$.

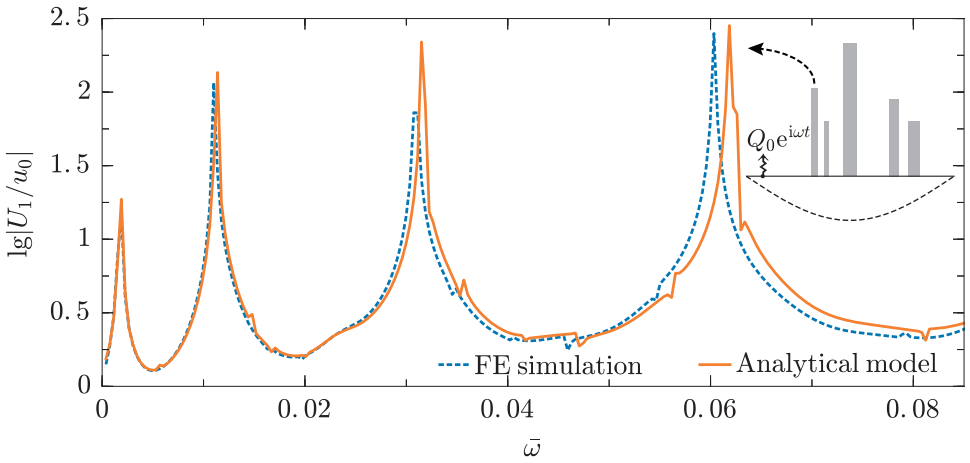

Figure 5. Horizontal response spectrum at the free end of the first plate $U_1(h_1)$.

in the spectrum, which evidence the mutual interactions among these plates [29]. The analytical solutions are again validated with FE simulations (the dashed line).

(c) Finite-size metasurfaces

We now consider the propagation of Rayleigh waves across a cluster of plates, i.e., a flexural metasurface. We aim to show the capability of the proposed formulation to reproduce the wave field in this complex configuration.

Thus, we consider an array of 30 identical plates ($l = 0.3\,\mathrm{m}$ and $h = 14\,\mathrm{m}$), which are arranged periodically with a lattice constant $L = 2\,\mathrm{m}$. A similar configuration was considered in Ref. [6] for Rayleigh waves interacting with rods. To predict the effect of flexural resonators on the propagation of Rayleigh waves, we first compute the dispersion relation for the infinite system. The dispersion relation can be obtained either analytically, by exploiting the thin-plates impedances, or via 2D FE models imposing periodic BCs, as shown in Figure 6a (more details on the computation can be found in the supplementary material).

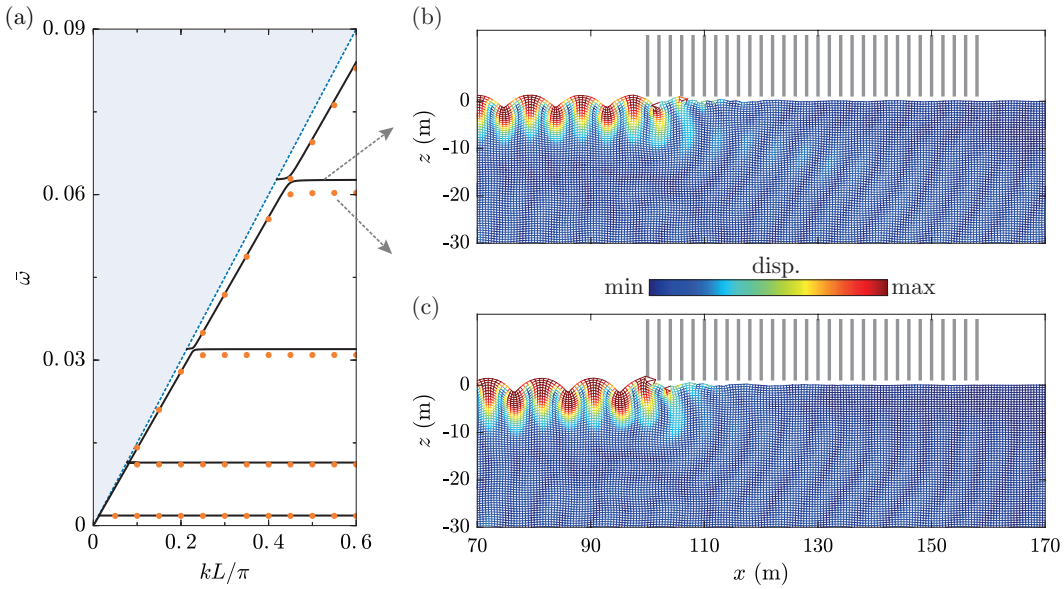

Figure 6. Rayleigh wave interacting with a metasurface atop an elastic half-space. (a) The dispersion curves for an infinite array of plates resting on the half-space ($L = 2$ m). Solid lines and circles denote, respectively, the analytical solution and the FE simulation, while the dashed line indicates the shear wave sound-line. (b) Analytical solution and (c) FE simulation of the wave field at the fourth flexural resonance for the half-space supporting a periodic array of $N = 30$ plates.

In particular, we show with solid black lines the solution obtained from the analytical dispersion equation (see the supplementary material) and with orange circles the dispersion relation calculated by FE. The dashed blue line indicates the shear wave sound-line. Overall, a good agreement is found between the analytical and FE computed dispersion curves. Note that, differently from a metasurface of longitudinal resonators [6], the bandgap induced by the plate flexural resonance is barely visible in this scenario. Indeed, the bandgap width is related to the slenderness of the plate as well as the stiffness ratio of the plate to the substrate. For further details, the reader can refer to [6,17]. Nevertheless, for incident waves at one of the plate resonance, we still expect a strong localization of the wave field at the onset of the metasurface, as a result of the interaction between the incident field and the plate flexural motion.

To visualize this phenomenon, we consider an incident Rayleigh wave at the fourth flexural resonance of the plate ($\bar{\omega} = 0.06$), which is excited by the source $Q_0 e^{i\omega t}$ placed 100 m away from the first plate. The wave field, calculated by (3.1*a*) and (3.1*b*), is displayed in Figure 6b and highlights the strong interaction between the Rayleigh waves and the plates. As shown in Figure 6c, the predicted wave field is in very good agreement with the one computed by using the FE simulation.

5. Conclusion

We have provided a multiple scattering formulation to investigate the interaction of Rayleigh waves with an array of thin plates located at the surface of an elastic half-space. The presence of the plates on top of the half-space is modelled by means of their equivalent impedances, derived by exploiting the Kirchhoff plate theory. The flexural motion of the plates, under the action of Rayleigh waves, provides additional scattered wave fields which are modelled invoking ad-hoc Green's functions. The amplitudes of the scattered wave fields are obtained from a multiple scattering formulation by imposing the continuity of displacement and slope at the footprint of the thin plates. Our approach enables the treatment of a flexural metasurface in an arbitrary way,

namely with no restriction on the mechanical and geometrical properties of the plates as well as in their spatial configuration. The capability of the method has been discussed by investigating a single and an array of thin plates atop a homogeneous half-space. The methodology can capture the interaction between the plate dynamics, mediated by the elastic substrate, and the complex wave patterns induced by the presence of multiple flexural resonators.

The advantages of the proposed semi-analytical formulation over a standard FE solution are not limited to the reduction of the computational effort. The major advantage of the multiple scattering technique stems from the possibility of computing the contribution of each scatter to the total wavefield. Evaluating and separating the contribution of each scatter to the overall dynamics of the metasurface open new paths towards the inverse design of scattering based devices, as demonstrated in recent works concerning the dynamics of metasurfaces over plates [36]. Similarly, in the context of structure-soil-structure interaction and urban vibration problem, it is beneficial to evaluate the contribution of each building to the wavefield and to assess, for example, the effect of a new construction on the response of existing buildings.

We recognize that the Kirchhoff-Love plate formulation used to model the flexural resonators neglects the shear deformation and the rotary inertia, resulting in discrepancies for higher modes. Nevertheless, the accuracy is sufficient to properly model the dynamics of the metasurface in the low-frequency regime, namely around the first flexural modes of the scatters. Finally, we envision that our formulation can be extended to deal with 3D problems. Note that, Green's functions for axial point/strip sources on a 3D half-space surface are readily available in Ref. [37]. Further efforts should be instead devoted to develop Green's functions for stress distributions generated by the flexural motion of beam-like resonators on a 3D half-space.

Data Accessibility. This article has no additional data. All the results displayed are obtained via the analytical formulation and the FE model detailed in the paper.

Authors' Contributions. **Xingbo Pu:** Conceptualization, Methodology, Investigation, Software, Writing - original draft. **Antonio Palermo:** Conceptualization, Investigation, Validation, Writing - review & editing, Co-supervision. **Alessandro Marzani:** Conceptualization, Investigation, Writing - review & editing, Supervision, Funding acquisition.

Competing Interests. The authors declare that they have no conflict of interest.

Funding. This project has received funding from the European Union's Horizon 2020 research and innovation programme under the Marie Skłodowska Curie grant agreement No 813424.

References

1. Hussein MI, Leamy MJ, Ruzzene M. 2014 Dynamics of phononic materials and structures: Historical origins, recent progress, and future outlook. *Applied Mechanics Reviews* **66**.
2. Liu Z, Zhang X, Mao Y, Zhu Y, Yang Z, Chan CT, Sheng P. 2000 Locally resonant sonic materials. *Science* **289**, 1734–1736.
3. Muhammad, Lim C. 2021 From photonic crystals to seismic metamaterials: A review via phononic crystals and acoustic metamaterials. *Archives of Computational Methods in Engineering* pp. 1–62.
4. Boechler N, Eliason J, Kumar A, Maznev A, Nelson K, Fang N. 2013 Interaction of a contact resonance of microspheres with surface acoustic waves. *Physical review letters* **111**, 036103.
5. Colombi A, Roux P, Guenneau S, Gueguen P, Craster RV. 2016 Forests as a natural seismic metamaterial: Rayleigh wave bandgaps induced by local resonances. *Scientific reports* **6**, 1–7.
6. Colquitt D, Colombi A, Craster R, Roux P, Guenneau S. 2017 Seismic metasurfaces: Sub-wavelength resonators and Rayleigh wave interaction. *Journal of the Mechanics and Physics of Solids* **99**, 379–393.
7. Palermo A, Celli P, Yousefzadeh B, Daraio C, Marzani A. 2020 Surface wave non-reciprocity via time-modulated metamaterials. *Journal of the Mechanics and Physics of Solids* **145**, 104181.
8. Raguin L, Gaiffe O, Salut R, Cote JM, Soumann V, Laude V, Khelif A, Benchabane S. 2019 Dipole states and coherent interaction in surface-acoustic-wave coupled phononic resonators. *Nature communications* **10**, 1–8.

9. Pu X, Palermo A, Cheng Z, Shi Z, Marzani A. 2020 Seismic metasurfaces on porous layered media: Surface resonators and fluid-solid interaction effects on the propagation of Rayleigh waves. *International Journal of Engineering Science* **154**, 103347.
10. Zeighami F, Palermo A, Marzani A. 2021 Rayleigh waves in locally resonant metamaterials. *International Journal of Mechanical Sciences* **195**, 106250.
11. Garova E, Maradudin A, Mayer A. 1999 Interaction of Rayleigh waves with randomly distributed oscillators on the surface. *Physical Review B* **59**, 13291.
12. Khelif A, Achaoui Y, Benchabane S, Laude V, Aoubiza B. 2010 Locally resonant surface acoustic wave band gaps in a two-dimensional phononic crystal of pillars on a surface. *Physical Review B* **81**, 214303.
13. Veres IA, Berer T. 2012 Complexity of band structures: Semi-analytical finite element analysis of one-dimensional surface phononic crystals. *Physical Review B* **86**, 104304.
14. Palermo A, Vitali M, Marzani A. 2018 Metabarriers with multi-mass locally resonating units for broad band Rayleigh waves attenuation. *Soil Dynamics and Earthquake Engineering* **113**, 265–277.
15. Wootton PT, Kaplunov J, Prikazchikov D. 2020 A second-order asymptotic model for Rayleigh waves on a linearly elastic half plane. *IMA Journal of Applied Mathematics* **85**, 113–131.
16. Wootton P, Kaplunov J, Colquitt D. 2019 An asymptotic hyperbolic–elliptic model for flexural-seismic metasurfaces. *Proceedings of the Royal Society A* **475**, 20190079.
17. Marigo JJ, Pham K, Maurel A, Guenneau S. 2020 Surface waves from flexural and compressional resonances of beams. *arXiv preprint arXiv:2001.06304*.
18. Palermo A, Marzani A. 2018 Control of Love waves by resonant metasurfaces. *Scientific reports* **8**, 1–8.
19. Fuentes-Domínguez R, Yao M, Colombi A, Dryburgh P, Pieris D, Jackson-Crisp A, Colquitt D, Clare A, Smith RJ, Clark M. 2021 Design of a resonant Luneburg lens for surface acoustic waves. *Ultrasonics* **111**, 106306.
20. Maurel A, Marigo JJ, Pham K, Guenneau S. 2018 Conversion of Love waves in a forest of trees. *Physical Review B* **98**, 134311.
21. Chaplain GJ, De Ponti JM, Colombi A, Fuentes-Dominguez R, Dryburg P, Pieris D, Smith RJ, Clare A, Clark M, Craster RV. 2020 Tailored elastic surface to body wave Umklapp conversion. *Nature communications* **11**, 1–6.
22. Colombi A, Colquitt D, Roux P, Guenneau S, Craster RV. 2016 A seismic metamaterial: The resonant metawedge. *Scientific reports* **6**, 1–6.
23. Ungureanu B, Makwana MP, Craster RV, Guenneau S. 2021 Localizing Elastic Edge Waves via the Topological Rainbow Effect. *Physical Review Applied* **15**, 014057.
24. Luco JE, Contesse L. 1973 Dynamic structure-soil-structure interaction. *Bulletin of the Seismological Society of America* **63**, 1289–1303.
25. Groby JP, Wirgin A. 2008 Seismic motion in urban sites consisting of blocks in welded contact with a soft layer overlying a hard half-space. *Geophysical Journal International* **172**, 725–758.
26. Boutin C, Roussillon P. 2006 Wave propagation in presence of oscillators on the free surface. *International journal of engineering science* **44**, 180–204.
27. Schwan L, Boutin C, Padrón L, Dietz MS, Bard PY, Taylor C. 2016 Site-city interaction: theoretical, numerical and experimental crossed-analysis. *Geophysical Journal International* **205**, 1006–1031.
28. Marigo JJ, Pham K, Maurel A, Guenneau S. 2020 Effective model for elastic waves propagating in a substrate supporting a dense array of plates/beams with flexural resonances. *Journal of the Mechanics and Physics of Solids* **143**, 104029.
29. Pu X, Palermo A, Marzani A. 2021 Lamb's problem for a half-space coupled to a generic distribution of oscillators at the surface. *International Journal of Engineering Science* **168**, 103547.
30. Lamb H. 1904 I. On the Propagation of Tremors over the Surface of an Elastic Solid. *Philosophical Transactions of the Royal Society of London. Series A, Containing papers of a mathematical or physical character* **203**, 1–42.
31. Achenbach J. 1973 *Wave propagation in elastic solids*. New York: American Elsevier Publishing Company, Inc.
32. Philippacopoulos A. 1988 Lamb's problem for fluid-saturated, porous media. *Bulletin of the Seismological Society of America* **78**, 908–923.
33. Zheng P, Zhao SX, Ding D. 2013 Dynamic Green's functions for a poroelastic half-space. *Acta Mechanica* **224**, 17–39.

34. Arcos R, Romeu J, Clot A, Genesca M. 2013 Some analytical aspects of viscoelastic Lamb's problem for improving its numerical evaluation. *Wave Motion* **50**, 226–232.
35. Woods RD. 1968 Screening of Surface Wave in Soils. *Journal of the Soil Mechanics and Foundations Division* pp. 951–979.
36. Packo P, Norris AN, Torrent D. 2019 Inverse grating problem: Efficient design of anomalous flexural wave reflectors and refractors. *Physical Review Applied* **11**, 014023.
37. Miller G, Pursey H. 1954 The field and radiation impedance of mechanical radiators on the free surface of a semi-infinite isotropic solid. *Proceedings of the Royal Society of London. Series A. Mathematical and Physical Sciences* **223**, 521–541.